Final Report
Stony Brook University

Up-Scaling Geochemical Reaction Rates for Carbon Dioxide (CO2) in Deep Saline Aquifers

Grant No. DE-FG02-05ER15635

W. Brent Lindquist
lindquis@ams.sunysb.edu

Department of Applied Mathematics and Statistics
State University of New York, Stony Brook, NY 11794-3600

Co-Investigators

Catherine A. Peters
cap@princeton.edu

Michael Celia
celia@princeton.edu

Department of Civil & Environmental Engineering
Princeton University, Princeton NY 08544

Unexpended Funds – Stony Brook:
A six month no-cost extension was requested by Stony Brook University. Funds unexpended by the end of the no-cost period: $0.00

This was a three year joint project between Princeton and SUNY Stony Brook.. The overall goal of the project was to bridge the gap between our knowledge of small-scale geochemical reaction rates and reaction rates meaningful for modeling transport at core scales. The working hypothesis was that reaction rates, determined from laboratory measurements based upon reactions typically conducted in well mixed batch reactors using pulverized reactive media may be significantly changed in *in situ* porous media flow due to rock microstructure heterogeneity. Specifically we hypothesized that, generally, reactive mineral surfaces are not uniformly accessible to reactive fluids due to the random deposition of mineral grains and to the variation in flow rates within a pore network. Expected bulk reaction rates would therefore have to be correctly up-scaled to reflect such heterogeneity.

The specific objective was to develop a computational tool that integrates existing measurement capabilities with pore-scale network models of fluid flow and reactive transport. The existing measurement capabilities to be integrated consisted of (a) pore space morphology, (b) rock mineralogy, and (c) geochemical reaction rates. The objective was accomplished by: (1) characterizing sedimentary sandstone rock morphology using X-ray computed microtomography, (2) mapping rock mineralogy using back-scattered electron microscopy (BSE), X-ray dispersive spectroscopy (EDX) and CMT, (3) characterizing pore-accessible reactive mineral surface area,

and (4) creating network models to model acidic CO_2 saturated brine injection into the sandstone rock samples.

The project had three distinct phases.

The first phase consisted of acquiring, imaging, and analyzing the pore network of 12 cores taken from the Viking Basin in Alberta Canada. There cores were extracted from 12 different well bores sampled over a large area of the basin. The cores were sub-cored with two sub-cores taken from each core. These cores were imaged vi X-ray computed micro-tomography (X-CMT) at 3.98 micron resolution at the X2B beam-line at the National Synchrotron Light Source at Brookhaven National Laboratory during two separate beam time allotments in the first years funding period. Three of the cores were unusable (two were too opaque for the ~34 keV maximum usable beam energy, one sample was too friable to sub-core). The networks as well as their statistical properties of the remaining 9 x 2 = 18 sub-core images were extracted using the 3DMA-Rock software package. The networks and their statistical properties provide necessary input for the generation of both actual as well as realistic, *random*, network model geometries. The results of this first phase of the work were presented in the first and second yearly progress reports (attached for convenience) – and we refer to them for details.

The second phase consisted of mapping mineral phases in these samples. Three samples were utilized for this work. These three samples 3W4, 10W4 and 14W5 represent, respectively, samples of sandstone, shaley sandstone, and conglomerate sandstone. The Princeton team generated wo dimensional mineral maps using backscattered electron imaging (BSE), a mode of scanning electron microscopy in which backscattered electrons are examined to provide mean atomic number (MAN) surface maps. The maps were obtained by sampling small surface areas. The BSE maps were used to divide minerals into three categories: the predominant matrix material – quartz, minerals having MAN less than that of quartz, and minerals having MAN greater than that of quartz. Fig. 1 shows the raw and processed images of one of the BSE maps from 14W5.

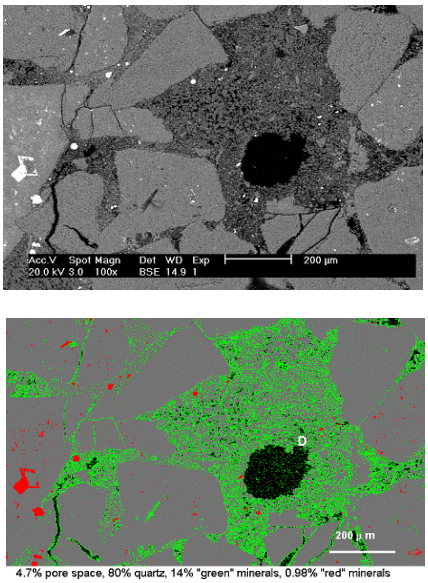

Figure 1. (top left) BSE maps on sandstone sample 14W5 and (bottom left) images segmented according to mean atomic number of material relative to quartz. Black: pore space; green: MAN < quartz; grey: quartz; red: MAN > quartz. Image width ~1.2 mm.

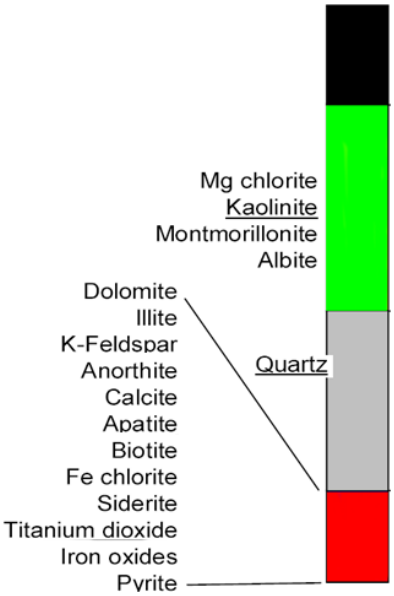

Figure 2. (right) EDX identification of the major minerals occupying each region of mean atomic number.

Energy dispersive X-ray spectroscopy (EDX), which is (comparative to BSE) time consuming, was used to provide identification of the predominant minerals in the latter two mineral categories. EDX has confirmed (Fig. 2) that the minerals with MAN less than that of quartz in these sandstone samples are primarily clays, with kaolinite being predominant. We therefore refer to the minerals in this MAN range collectively as "clay". The minerals with MAN larger that quartz are listed in Fig. 2. We refer to the minerals in this MAN range as "mineral of interest" (MoI).

The mineral maps have been used to understand the spatial patterns of reactive minerals and to statistically characterize pore-mineral contact [1-3]. The analysis has shown, for example [1], that kaolinite, which in sandstones is the primary authigenic clay mineral cementing quartz grains, can account for only 5% to 30% of mineral content, but accounts for 65% to 90% of pore-mineral contact boundaries. Thus, if a mineral volume fraction is used in reactive transport modeling as a proportional measure of accessible surface area in consolidated sandstones, the reaction rates are likely to be overestimated by factors of three to five.

The Stony Brook team has demonstrated (Fig. 3) that a mineral identification map analogous to BSE/mean atomic number can be performed on CMT images by segmenting on X-ray attenuation coefficient values. While the spatial resolution of CMT-based mineral distribution mapping is not as fine as BSE-based mapping, it has the advantage of producing a 3D map while BSE maps are restricted to 2D. There is also a difference in that CMT measures X-ray attenuation which is, at the energy range over which the NSLS beam lines operate, proportional to the cross section of the photoelectric effect, which in turn depends nonlinearly on (a power of) atomic number. From the list of minerals involved in these sandstones (from the EDX analysis) we have determined that those minerals with MAN less than that of quartz will also have computed tomography values less than that of quartz, while those minerals with MAN greated than that of quartz will also have computed tomography values greater than that of quartz. Thus the set of minerals lying in the respective (MAN vs. computed tomography values) ranges relative to quartz will be the same under both CMT and BSE analysis.

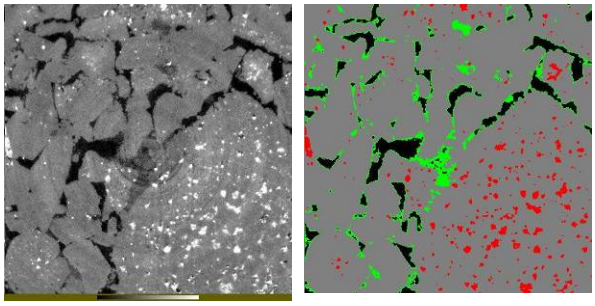

Figure 3. (left) Single slice from a CMT image of the sandstone 14W5. (right) Analog of the segmentation performed on the BSE image in Fig. 1 using CMT attenuation coefficient values. Slice dimensions are 3 mm x 3 mm. Black – pore. Green - clay. Grey – quartz. Red – MoI.

Algorithms were added to the 3DMA-Rock software package to perform the mineral maps and to compute surface areas between any two phases identified by these mineral distribution maps. Table 1 compares the results of BSE and CMT mineral maps. In general the results are reasonably good. Partial differences can certainly be accounted for by the difference in pixel/voxel size between the two techniques (1.8 μm for BSE, 3.98 μm for CMT), the 2D vs. 3D

difference in the techniques, the amount of area/volume sampled and the particular region sampled.

		Porosity (%)	Mineral abundances (%)			Mineral accessibilities (%)		
			clays	quartz	MoI	clays	quartz	MoI
Sandstone	BSE	18	21	73	6	81	17	2
	CMT	14	15	82	3	63.4	35.3	1.3
Shaly sandstone	BSE	7	31	64	5	86	13	1
	CMT	4	10	89	1	69.8	29.5	0.7
Conglomerate sandstone	BSE	8	5	94	1	65	35	<1
	CMT	7	3	95	2	52.3	46.4	1.3

Tab le 1. Comparison between BSE and CMT mineral maps. Clays: minerals with MAN < quartz. MoI: minerals with MAN > quartz. Abundance: percent of total solid volume occupied by mineral. Accessibility: percent of pore-grain surface area accounted for by mineral.

The third phase consisted of the development of network flow models to simulate acidic CO_2 saturated brine injection into the sandstone rock samples. The models build upon the initial work of Li *et al.* [4, 5] which examined such flow in model media based upon a rectangular lattice of pores. The Li *et al.* model is a system of 11 reactions, 9 of which are purely aqueous and are modeled as instantaneous (relative to the time scales of the convective flow) and 2 of which involve solid species and are modeled dynamically. These latter two reactions involve the interaction of the clay kaolinite (1K) and the feldspar anorthite (1A) with the acidic brine:

$$\mathrm{Al_2Si_2O_5(OH)_4(s) + 6H^+ \leftrightarrow 2Al^{3+} + 2H_4SiO_4 + H_2O}, \qquad (1K)$$

$$\mathrm{Ca_2Al_2Si_2O_8(s) + 8H^+ \leftrightarrow Ca^{2+} + 2Al^{3+} + 2H_4SiO_4}. \qquad (1A)$$

The laboratory determined rates [mol/m^{2}s] for these reactions are, respectively:

$$r_K = \left(k_{H.K}\left\{H^+\right\}^{0.4} + k_{OH,K}\left\{OH^-\right\}^{0.3}\right)\left(1-\Omega_K^{0.9}\right), \quad \Omega_K = \frac{\left\{Al^{3+}\right\}^2\left\{H_4SiO_4\right\}^2}{\left\{H^+\right\}^6 K_{eq,K}}, \qquad (2K)$$

$$r_A = \left(k_{H,A}\left\{H^+\right\}^{1.5} + k_{H_2O,A} + k_{OH,A}\left\{OH^-\right\}^{0.33}\right)\left(1-\Omega_A\right), \quad \Omega_A = \frac{\left\{Ca^{2+}\right\}\left\{Al^{3+}\right\}^2\left\{H_4SiO_4\right\}^2}{\left\{H^+\right\}^8 K_{eq,A}}. \qquad (2A)$$

Here the k are reaction rate constants [mol/m^{2}s], and $\{\alpha\}$ represent (dimensionless) chemical activities, which are related to concentrations $[\alpha]$ via $\{\alpha\} = \gamma\,[\alpha]/[\alpha]_0$, where γ is an activity coefficient and $[\alpha]_0$ is a reference concentration. We assume dilute solutions, so the reference

concentration for each aqueous species is 1 M. As the rates in (2) are determined from well-mixed batch reaction experiments, we assume these rates hold at the sub-micron scale – and use them for the reactions occurring locally within a single pore. Table 2 summarizes the values of the reaction constants appearing in (2).

species	$\log_{10}K_{eq}$	$\log_{10}k_H$	$\log_{10}k_{H2O}$	$\log_{10}k_{OH}$
kaolinite	3.80	-10.40	NA	-15.30
anorthite	21.7	-3.07	-11.35	-13.25

Table 2. Equilibrium and reaction rate constants at 50°C

The sign of the reaction rate (from equations (1): positive for dissolution, negative for precipitation) is determined by the term $1-\Omega$, i.e. by the magnitude of the saturation state, Ω. $\Omega < 1$ denotes dissolution, $\Omega > 1$ denotes precipitation. The dissolution/precipitation status is somewhat more intuitively expressed by the saturation index, $SI \equiv \log \Omega$ which will then be negative for dissolution and positive for precipitation.

For later use, we note that the equations in (2) are of the form

$$r = r_{pH} \times f_{\Omega} . \tag{3}$$

The f_{Ω} term represents the $(1-\Omega^p)$ term in each equation; it reflects the extent of the dissolution/precipitation deviation from equilibrium of the reaction. The r_{pH} term depends solely on reaction coefficients and H^+, OH^- activities, and therefore reflects the pH dependence of the reaction rate.

$H_2O \leftrightarrow H^+ + OH^-$	$H_4SiO_4 \leftrightarrow H_3SiO_4^- + H^+$	$Al^{3+} + 2OH^- \leftrightarrow Al(OH)_2^+$
$H_2CO_3 \leftrightarrow HCO_3^- + H^+$	$H_3SiO_4^- \leftrightarrow H_2SiO_4^{2-} + H^+$	$Al^{3+} + 3OH^- \leftrightarrow Al(OH)_3$
$HCO_3^- \leftrightarrow CO_3^{2-} + H^+$	$Al^{3+} + OH^- \leftrightarrow Al(OH)^{++}$	$Al^{3+} + 4OH^- \leftrightarrow Al(OH)_4^-$

Table 3. Instantaneous reactions considered by the Li *et al.* model.

Table 3 presents the aqueous system of instantaneous reactions. Including H_2O, there are 15 aqueous species (see Table 3 and system (1)) whose concentrations must be tracked in time in each pore in the network models. Each of the 15 species concentrations in each pore, *i*, are moved convectively and diffusively via the ODE

$$V_i \frac{d[\alpha]_i}{dt} + \sum_{Q_{ij}>0} Q_{ij}[\alpha]_i + \sum_{Q_{ij}<0} Q_{ij}[\alpha]_i = S_{i,\alpha} + \sum_j D_\alpha a_{ij} \frac{[\alpha]_j - [\alpha]_i}{l_{ij}} , \tag{4}$$

where: *j* indexes the neighboring pores; V_i is the volume of pore *i*; $[\alpha]_i$ is the concentration of species α in pore *i*; D_α is the diffusion coefficient of species α; Q_{ij} is the volume flow rate between pores *i* and *j*; a_{ij} is the area of the throat between pores *i* and *j*.

$S_{i,\alpha}$ is the reaction source term of species α in pore *i*. It has units of mol/sec and represent mass change rate. $S = 0$ for the 10 species not contributing directly to system (1). For H^+, $S_{i,H+} = -8r_A A_A - 6r_K A_K$; for Ca^{2+}, $S_{i,Ca2+} = r_A A_A$, where A_K (A_A) is the accessible surface area of koalinite (anorthite) in pore *i*. The value for *S* for the remaining 3 aqueous species is determined analogously.

Equation (4) is integrated via 4'th order Runge-Kutta. As solution of (3) does not guarantee that species remain in equilibrium, equilibrium is enforced following each Runge-Kutta time-step by simultaneous solution of the 9 reaction equations in Table 3 augmented by 6 conditions enforcing conservation of total concentrations for six of the independent species. (We chose H_2O, H^+, H_2CO_3, H_4SiO_4, Al^{3+} and Ca^{2+}.) This non-linear system is solved via Newton-Raphson.

Our reactive network flow models were developed based upon the Viking sandstones, using the exact pore and mineral phase structure. Models were developed for three of the sub-cores: 3W4, 10W4 and 14W5. Each model simulated a volume of 2.9×2.9×2.4 mm^3. For simplicity, the entire "clay" phase identified in the CMT mineral maps for these three cores was modeled as kaolinite while the MoI phase was assumed to be anorthite. The accessible surface areas for anorthite and kaolinite in each pore are available from the CMT mineral maps obtained for each core.

The flow rates, Q_{ij}, were determined by a single-phase flow model (solute concentrations were assumed not to affect aqueous flow rates). We used the network model of Patzek [6] which computes pore-to-pore conductance based upon cross sectional shape factor values assuming (based upon shape factor magnitude) either triangular, rectangular, circular cross sectional shape of the connecting channel. In our model, determinations of shape factor came from the accurately (4 micron resolution) measured cross sectional shape of the throats connecting between pores.

The initial conditions in each core were modeled as saline water, pH 6.6, with total dissolved solids of 0.45M ($[Na^+] = [Cl^-] = 0.45M$). For equilibrium of the saline water with quartz and kaolinite, the initial pore solution also had $[Ca^{2+}] = 7.9x10^{-6}$ M. Acidic saline solution ($[Na^+] = [Cl^-] = 0.45M$, $[Ca^{2+}] = 7.9x10^{-6}$ M) with dissolved CO_2 was injected at two different flow rates. The concentration of H_2CO_3 in the injection solution was determined by the solubility of CO_2 (1.01M) at a pressure of 100 bar and temperature of 50°C. The remaining species in the injected solution are determined from Table 3 and the condition that their concentrations are in equilibrium with that of H_2CO_3. The pH of the injection solution is 3.01.

From the network model, the mass changes $M_{K,i}$ [mol/s] of kaolinite and $M_{A,i}$ of anorthite can be computed for each pore *i. Effective* (up-scaled) reaction rates, R_N [mol/m^2s], for the entire core (pore-network) can be defined by

$$R_{N,K} = \frac{\sum_i M_{K,i}}{\sum_i A_{K,i}}, \qquad R_{N,A} = \frac{\sum_i M_{A,i}}{\sum_i A_{A,i}}. \tag{5}$$

The rates, R_N , are true, up-scaled reaction rates for the core accounting for all network, flow and mineral heterogeneities captured by the network flow model.

We contrast these true rates against a common attempt at up-scaled rates using volume-averaged concentrations. Let

$$\overline{[\alpha]} = \frac{\sum_i [\alpha]_i V_i}{\sum_i V_i}, \tag{6}$$

denote the core-averaged concentration of species α. From these, core-averaged activities can be computed by $\overline{\{\alpha\}} = \gamma \overline{[\alpha]}$ (where we again assume a reference core-averaged concentration of 1M). *Volume-averaged* reaction rates can be defined from (2) by

$$\overline{R}_K = \left(k_H \overline{\{H^+\}}^{0.4} + k_{OH} \overline{\{OH^-\}}^{0.3} \right) \left(1 - \overline{\Omega}_K^{0.9} \right), \tag{7K}$$

$$\overline{R}_A = \left(k_H \overline{\{H^+\}}^{1.5} + k_{H_2O} + k_{OH} \overline{\{OH^-\}}^{0.33} \right) \left(1 - \overline{\Omega}_A \right), \quad . \tag{7A}$$

where the volume-averaged saturation rates $\overline{\Omega}$ are also computed from (2) using volume averaged activities.

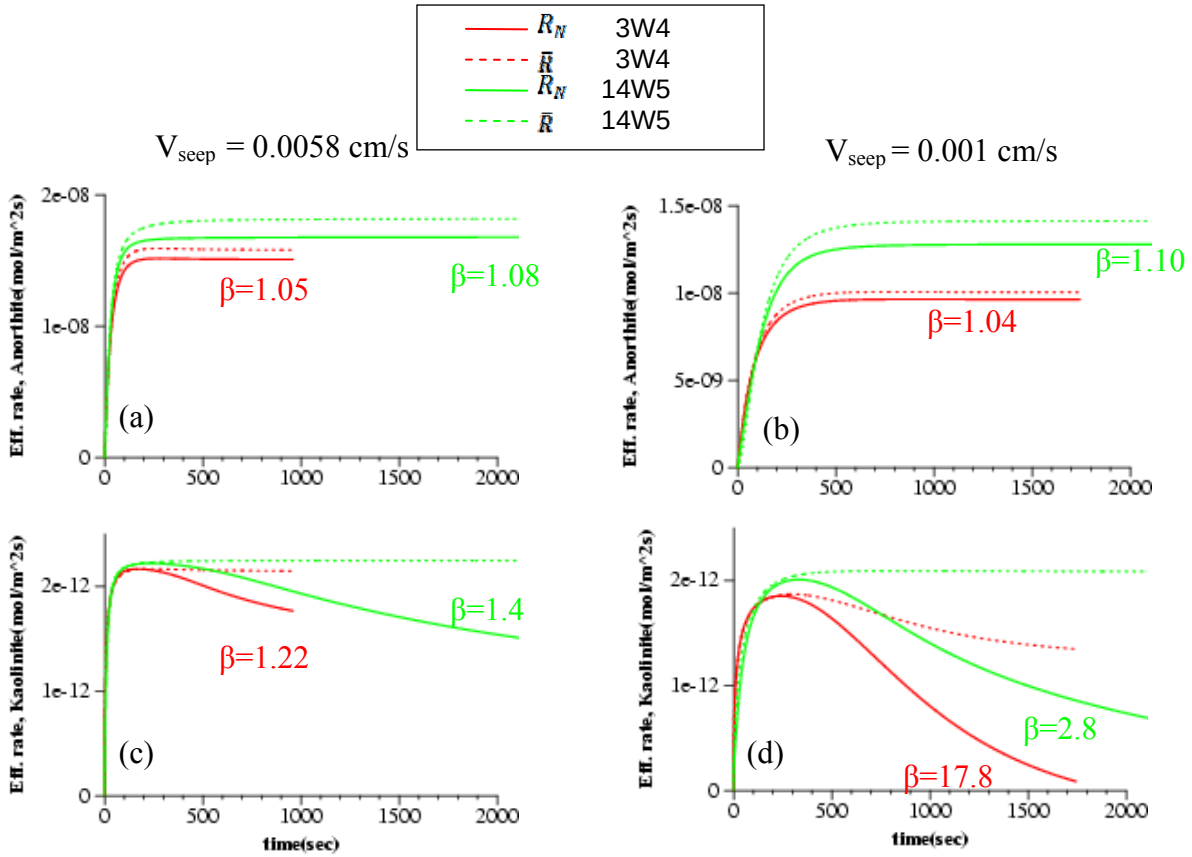

Figure 4. Comparison of true and volume-averaged core-scale reaction rates computed for anorthite (a)-(b) and kaolinite (c)-(d) reactions in two of the network flow models (the 3W4 and 14W5 cores) for two different injection flow rates corresponding to average seepage rates of 0.0058 and 0.001 cm/s. The β values quoted are for the end-point values.

We characterize discrepancy between that true and volume-averaged up-scaling methods by considering the ratios

$$\beta_K \equiv \overline{R_K} / R_{N,K} \text{ and } \beta_A \equiv \overline{R_A} / R_{N,A}. \quad (8)$$

Fig. 4 summarizes the results of the network flow models for two of the rock samples, the sandstone 3W4 and the conglomerate sandstone 14W5. The models were each run at two difference injection rates, corresponding to average seepage rates of 0.0058 and 0.001 cm/s. Each graph presents bulk reaction rates as a function of time for a given combination of species (kaolinite, anorthite) and flow rate. In order to reduce computational times, simulations were run either until steady state in the bulk rates were clearly demonstrated, or clear differences between bulk and volume-averaged rates were established. Both the true, R_N, and the volume-averaged, $\overline{R}$, reaction rates for both sandstone models are presented on each graph. For anorthite, at both fast and slow flow rates, (top left and right graphs) a steady state bulk reaction rate is achieved after a few minutes of flow with the steady state volume averaged reaction rate being in close agreement with the true rate. The situation is different for kaolinite. At the faster flow rate (bottom left graph) the volume averaged method predicts a steady state reaction rate is achieved in both cores. However the true bulk reaction rate continues to decrease over the full simulation time. At the slower injection rate (bottom left) the volume averaged reaction rate reaches steady state only in the conglomerate sandstone. Again the true bulk reaction rates continue to decrease with time and there is a growing, significant discrepancy between the true and volume-averaged bulk reaction rates.

Understanding the scale-up results in Fig. 4 requires understanding (the pore network variation of) the behavior of system (2) for the true up-scaled rate and the behavior of the volume-averaged rate given by system (7).

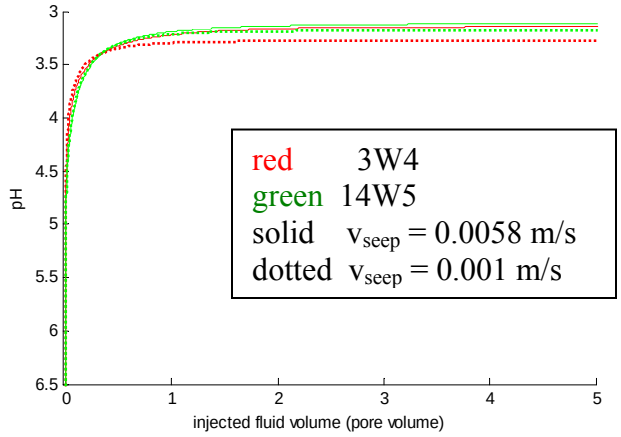

Figure 5. Average pH in the network flow models are a function of time – measured as injected pore volumes. (***Inverted y-axis of graph to show pH falls to acidic values.)***

We discuss the behavior of the volume-averaged reaction rates (7) first. The independent variables in (7) are the volume averaged specie activities, and the behavior of $\overline{R}$ depends on the behavior of the factors r_{pH} and f_Ω on the average activities. Initially, for all flow rates, all

sandstone samples, the reactive flow is dominated by the sweeping pH change through the system. Fig. 5 (replace with plot showing decile changes?) shows the average pH as a function of time. The pH falls and equilibrates throughout the network very rapidly to an acidic value. From reactions (7) and the reaction rate constants given in Table 2, it is seen that the $k_{H,A}\{H^+\}^p$ term (i.e. the pH) dominates the term r_{pH}, which in turn dominates the early time behavior of $\overline{R}$. With the pH equilibrated (at around ~ 1 PV of injected fluid), the continued behavior of $\overline{R}$ depends solely on f_Ω. We consider separately the anorthite and kaolinite reactions. Fig. 6 shows the large-time distribution of saturation index values (log Ω_A) in the pore network for the anorthite reaction. The large value of the equilibrium coefficient K_{eq} for the anorthite reaction, the acidic conditions, results in very negative values of SI_A (including its average value) with the consequence that $\overline{\Omega}_A \approx 0$ and $f_{\Omega_A} \sim 1$. Thus $\overline{R}_A$ remains constant once the pH equilibrates.

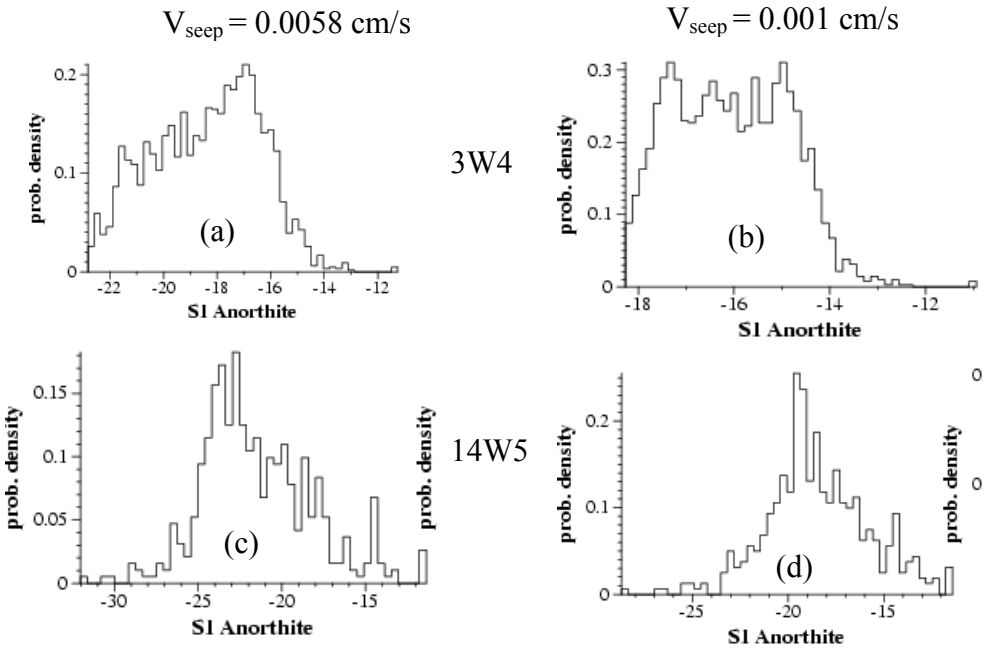

Figure 6. Distributions of the saturation index for the anorthite reaction in the pores of the 3W4 (a), (b) and 14W5 (c), (d) models at the final computational time for the fast (a), (c)) and slow (b), (d) injection rate simulations.

The situation for the kaolinite reaction is slightly different. Fig. 7 shows the large-time distributions of SI_K. The distribution averages for 14W5 – both flow rates, and for 3W4 – fast flow rate – remain relatively large and negative in value. Hence $\overline{\Omega}_K \approx 0$ and $f_{\Omega_K} \sim 1$. However, the average SI_K value for 3W4 – slow flow rate is closer to 0, implying that $\overline{\Omega}_K \leq 1$ and f_{Ω_K} decreases from one – hence the falling behavior noticed in $\overline{R}_K$ for the slow injection rate in 3W4 in contrast to the faster injection rate, or for the 15W4 flows. ***What remains to be understood in the velocity dependence of 3W4 and (apparently not) 14W5. hypothesis: slower flow is needed for 14W5 to show this effect. Note porosity difference between the two samples.***

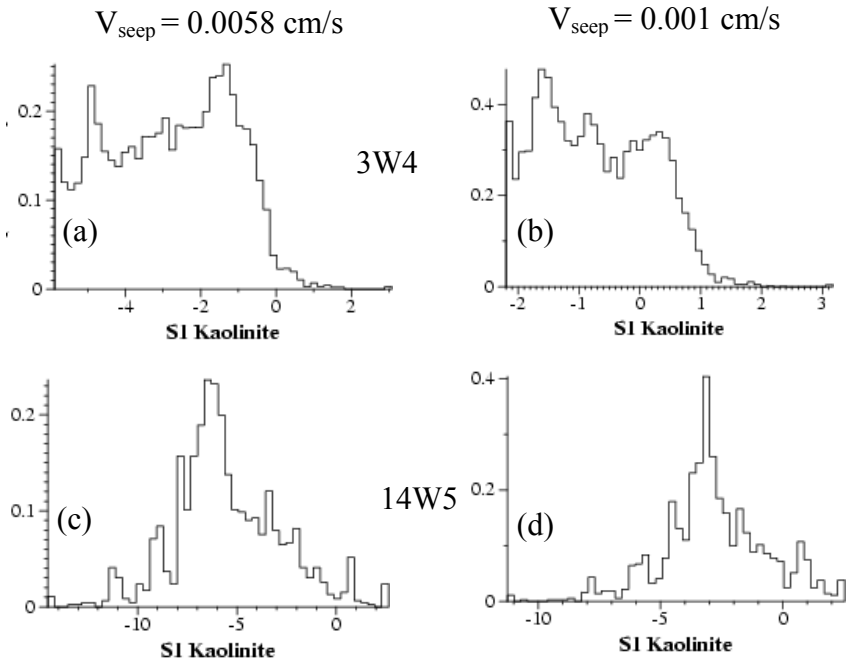

Figure 7. (***Redraw on same scale.***) Distributions of the saturation index for the kaolinite reaction in the pores of the 3W4 (a), (b) and 14W5 (c), (d) models at the final computational time for the fast (a), (c) and slow (b), (d) injection rate simulations.

We now consider the observed behavior of the true, up-scaled, reaction rate R_N whose behavior must be understood in terms of the rate of total mass production on all pores in the network (and not just by average values). Again, for all injection rates, rock samples and reaction types, the initial time behavior is dominated by the rapidly falling pH throughout the network which makes the r_{pH} dominant in all pores and the initial-time behavior of R_N reflect increasing r_{pH} value. For behavior after the pH equilibrates throughout the network (that is after ~1 PV injecting, Fig. 5), we consider the anorthite and kaolinite reactions separately. For anorthite, the (late-time) SI distribution in Fig. 6 explains the observed behavior. Unlike $\overline{R}_A$, the behavior of $R_{N,A}$ depends on the entire distribution of SI values. However all SI values remain large and negative, with the consequence that Ω_A is everywhere small, $f_{\Omega_A} \sim 1$ everywhere and $R_{N,A}$ remains constant. For $R_{N,K}$, the situation is markedly different. Consider the SI_K distributions in Fig. 7. A a majority of the pores the SI value is negative but there are a number of pores comprising the "tail" of the distribution where SI values are positive. In these latter pores Ω_K values fall either in the range [1, 100] (Fig. 7 (a)-(c)) or in the range [1, 1000] (Fig. 7(d)). Equation (1K) governs the rate of dissolution or precipitation of kaolinite in each pore. As the r_{pH} term is constant in each pore (pH has equilibrated), the dissolution/precipitation of kaolinite in each pore is controlled solely by the f_Ω term. *The (molecular-scale determined) form of f_Ω insures (for all practical purposes) that the dissolution mass rate is constant regardless of how large and negative the SI value is, while the precipitation rate grows exponentially for positive SI values).* Thus $R_{N,K}$ is dominated by the small fraction of pores in which precipitation is occurring. Thus $R_{N,K}$ decreases with time once the pH in the network has equilibrated.

Building on the work of Li *et al.*, this funded work has clearly demonstrated the need for appropriate scaling models to reflect accurate up-scaling from pore-to-core scales.

Next Steps

Ongoing computational work is required.

It would be useful to isolate the effects of the two reactions separately. These would provide benchmarks for comparison of the combined reaction. Computations should be performed: 1) assuming no anorthite is present (or accessible) in the sample (no MoI) and 2) assuming no kaolinite is present (no clay phase).

Computations need to be performed over a wider range of injection velocities (variation of Peclet numbers) in order to quantify the velocity dependence of the correctly upscaled bulk reaction rate.

Currently no physical change in porosity is implemented in the model. The model therefore does not capture the important topological changes that reactions produce – with expected impact on upscaled reaction rates. In work with PNNL we have demonstrated that a 4% porosity reduction (35% to 31%) due to secondary precipitation can lead to a 40% reduction in flow rate (under constant injection conditions). Algorithms for incorporating physical change due to dissolution and precipitation need to be included in the models.

References

1. Peters, C.A., *Accessibilities of reactive minerals in consolidated sedimentary rock: A BSE imaging study of three sandstones.* Chemical Geology, 2008.
2. Peters, C.A., J.A. Lewandowski, M.L. Maier, M.A. Celia, and L. Li, *Mineral grain spatial patterns and reaction rate up-scaling.*, in *XVI International Conference on Computational Methods in Water Resources*. 2006: Copenhagen, Denmark.
3. Peters, C.A. and M.L. Maier, *Backscatter electron imaging of Viking sandstones for mapping reactive minerals.* EOS Transactions of the AGU, 2006. **87**(52).
4. Li, L., C.A. Peters, and M.A. Celia, *Upscaling geochemical reaction rates using pore-scale network modeling.* Advances in Water Resources, 2006. **29**: 1357-1370.
5. Li, L., C.A. Peters, and M.A. Celia, *Applicability of averaged concentrations in determining geochemical reaction rates in heterogeneous porous media.* American Journal of Science, 2007. **307**: 1146-1166.
6. Patzek, T.W., *Verification of a complete pore network model of drainage and imbibition.* Society of Petroleum Engineers Journal, 2001. **6**(3): 144-156.

Publications

The following publications were supported entirely, or in part, by this grant.

Kim, D.; C. A. Peters; W. B. Lindquist. In preparation. “Mineral accessibilities and pore networks in sandstones via computed tomography”.

Kim, D.; C. A. Peters; W. B. Lindquist. In preparation. “Upscaling geochemical reaction rates in sandstones: pore to core”.

Li, L.; C. A. Peters; M. A. Celia. 2006. “Upscaling geochemical reaction rates using pore-scale network modeling” *Advances in Water Resources* 29: 1351-1370.

Li, L.; C. A. Peters; M. A. Celia. 2006. “Reply to ‘Comment on upscaling geochemical reaction rates using pore-scale network modeling’ by Peter C. Lichtner and Qinjun Kang”, *Advances in Water Resources*. In Press.

Li, L.; C. A. Peters; M. A. Celia. 2006. “The Effects of Mineral Spatial Distribution on Reaction Rates in Porous Media”, *Water Resources Research*. In Press.

Binning, P.J., M.A. Celia, and L. Li, "Pseudokinetics arising from the Upscaling of Equilibrium", in Proceedings of the XVI International Conference on Computational Methods in Water Resources, edited by Philip J. Binning Peter Engesgaard, Helge Dahle, George F. Pinder and William G. Gray. Copenhagen, Denmark, June, 2006 (http://proceedings.cmwr-xvi.org).

Peters, C. A., J. A. Lewandowski, M. L. Maier, M. A. Celia, L. Li. 2006. Mineral Grain Spatial Patterns and Reaction Rate Up-Scaling. Proceedings of the XVI International Conference on Computational Methods in Water Resources, edited by P. J. Binning, P. K. Engesgaard, H. K. Dahle, G. F. Pinder and W. G. Gray. Copenhagen, Denmark, June, 2006. Permanently archived at http://proceedings.cmwr-xvi.org.

W.B. Lindquist. The geometry of primary drainage. *J. Colloid Interf. Sci.*, 296(2) (2006) 655-668.

M. Prodanovic, W.B. Lindquist and R.S. Seright. Porous structure and fluid partitioning in polyethylene cores from 3D X-ray microtomographic imaging. J. Colloid Interf. Sci., 298(1) (2006) 282-297.

M. Prodanovic, W.B. Lindquist and R. Seright. Residual fluid blobs and contact angle measurements from X-ray images of fluid displacement. Proceedings, International Conference on Computational Methods in Water Resources XVI, Copenhagen, Denmark, June 19-22, 2006.

L. Li, C. A. Peters, M. A. Celia. 2005. “Scaling of geochemical reaction kinetics in heterogeneous porous media using pore-scale network modeling” American Geophysical Union 2005 Fall Meeting, San Francisco. EOS Trans. AGU 86(52), Fall Meeting Supplement, Abstract B32B-04.

Progress Report
2/1/05 to 1/31/06

Up-Scaling Geochemical Reaction Rates for Carbon Dioxide (CO2) in Deep Saline Aquifers

Grant No. DE-FG02-05ER15635

W. Brent Lindquist
lindquis@ams.sunysb.edu

Department of Applied Mathematics and Statistics
State University of New York, Stony Brook, NY 11794–3600

Unexpended Funds: Funds unexpended by 2/1/2006: $642.00.

Contents

1 Progress Report

1.1 Scale-Up of Geochemical Reaction Rates.

The first year milestones involve technical accomplishments. Six of the seven first year milestones have been accomplished as of the date of this report. The technical issues and the milestones (in italics) are discussed below.

It is necessary that the output from Stony Brook's 3DMA-Rock image analysis program used to generate pore networks, conform to input requirements for the Princeton network flow model. In consequence, *1) we have converted the 3DMA-Rock network output to a format appropriate for the Princeton network flow model.*

The use of core samples from a field site, that is a candidate site that may be used for CO_2 sequestration, is important for the scientific objectives of this work. While core samples from the Viking Basin in Alberta, Canada, are being processed to obtain pertinent networks, development of the Princeton network flow code must continue, using realistic sandstone networks. This was ensured by *2) transferring to Princeton, non-Alberta sandstone networks* consisting of one network derived from a Berea core (20% porosity) and four networks derived from Fontainebleau cores (7.5% to 22% porosity), previously analyzed at Stony Brook.

In preparation for image analysis of samples from the Viking basin, beam time at the National Synchrotron Light Source and BNL had to be arranged. *3a) A user's proposal, generated in May 2005, for beam time during the Sept-Dec '05 cycle resulted in two 5-day beam-time allocations, Sept. 21-25 and Oct 26-30, on the X2B beam-line maintained by Exxon.*

Twelve, two inch diameter siliclastic core samples from the Viking basin were provided by Dr. M. Buschkuehle of the Alberta Geological Survey (Table 1). The cores were taken from active and abandoned gas production wells, and abandoned and suspended injection wells, throughout the Viking basin *3b) The cores were prepared for imaging* by extracting subcores of 7 mm diameter. Due to brittleness, two samples would not produce sub-cores. The remaining samples produced sub-cores of various lengths. Generally two or three usable cores were extracted from each sample.

As expected, producing images with 1024^2 voxel slices (1800 projections per image) at 4 micron resolution, enables one image to be taken per 12-hour beam injection cycle at the NSLS. *3c) Thus during the 5-day beam allocation in Sept. 10 images were acquired, at a resolution of 3.98 microns.* Image sizes are $723 \times 723 \times 600$ voxels ($2.88 \times 2.88 \times 2.39$ mm^3). One sample contained large amounts of strongly attenuating non-silicate impurity. Given the 7 mm sample thickness of the subcores, we were unable to obtain a contrastible image for this sample at the energy available (33 kev maximum) at X2B. Thus single images were taken from 8 different samples and two images were taken from the nineth.

This report is being written during the Oct. beam allocation cycle. This cycle is devoted to producing additional images from those subcores not imaged in the Sept. allocation. Again, image acquisition is at the rate of 1 sample per

Table 1: The nine Viking field core samples successfully imaged during this first year.

core	depth extracted	rock type	well
3W4	2289 ft	sandstone	abnd gas
6W5	8523 ft	conglomerate and sandstone	abnd gas
7W4	806.5 m	sandstone	abnd inj
10W4	1531 ft	shaley sandstone	abnd gas
14W5	5128-5129 ft	conglomeratic sandstone	abnd inj
19W4	1243 m	sandstone	gas
19W5	5128 ft	sandstone	gas
20W4	3178-3181 ft	sandstone	abnd oil
24W4	4618 ft	sandstone	susp inj

12 hour beam cycle.

Further analysis of the core samples at Princeton involves X-ray powder diffraction and electron probe microanalysis to determine mineral content and distribution, as well as mercury porosimetry and nitrogen gas adsorption to produce respective measurements of effective pore radius distribution and specific surface area (as well as overall porosity). These latter two measurements are also provided by the 3DMA-Rock imaging software and will produce independent verification of the 3DMA-Rock results. *4) The bulk cores from which sub-cores were extracted were shipped to Princeton for these further analyses.* The actual imaged sub-cores will be made available to Princeton at the end of the first year imaging cycles.

Computation of grain surface area for pore bodies is important for surface reaction accuracy in the network flow model. *5) The 3DMA-Rock code has been upgraded to compute surface area for each pore body identified* using the marching cubes algorithm which provides a reliable triangulated surface from which to measure area. Fig. 2 demonstrates the distribution of pore surface area determined from one of the two image regions from Viking basin sample 19W5.

6) Network analysis of the 10 images obtained in the Sept. run is progressing and is expected to be finished within the three months remaining in year 1 of this project. Fig. 3 demonstrates the distributions for pore coordination number and volume as well as throat area obtained from the network computed from one image from core sample 19W6. The pore surface area distribution for this sample was displayed in Fig. 2.

The final milestone for year one, *7) comparison of the pore size and surface area distributions shown in Figs 3 and 2* with mercury porosimetry and nitrogen gas adsorption analyses awaits completion of these tests at Princeton. A Princeton graduate student has been recruited to complete these analyses.

1.2 Arc-Meniscus Configuration in Primary Drainage.

Our interest in the distribution of fluids at the pore scale, which is reflected both in the current funded project as well as in our previous DOE funded project, "Pore Scale Geometric and Fluid Distribution Analysis", had brought the following problem to our attention. An inherent requirement of multiphase flow network models is the ability to compute entry pressure conditions through throat connections into pore bodies in either drainage or wetting displacements. This problem is essentially that of computing entry pressure conditions into capillary tubes of arbitrary cross section shape. Solution of the entry pressures also requires computation of the configuration of wetting films in the capillary tube cross section. In the cross section, the wetting film configurations are described by the interface between the wetting and non-wetting fluids. This interface is the union of so-called "arc menisci". Wetting film configuration provides feedback to network flow models, as wetting films provide critical pathways for wetting fluid movement, play important roles in trapping behavior, and determine the extent of grain surface contacted for reactions involving the wetting fluid.

Network flow models utilize analytic solutions for entry pressure. Such solutions are obtained from the MS-P theory of Mayer, Stowe and Princen. Historically, the MS-P equation was solved for special cross sectional shapes. With regards to network flow modeling, the significant solution was for irregularly shaped triangular tubes and regular convex polygons. Triangular and rectangular cross sections have since dominated network flow models. In particular, the appearance of a shape factor parameter in the solution to the MS-P equation for regular convex polygons has prompted fitting network flow model cross sections to shape factor measurements. While solutions for cross sections of irregular polygon shape have been attempted, they have been restricted to the assumption that each arc meniscus in the solution corresponds to at most one polygon vertex. This condition will not be true in general for solutions to the MS-P equation for non-triangular, irregular convex polygons, and will certainly fail for most non-convex polygons.

In work during the first 6 months of this funded period, I have overcome this restriction and demonstrated how to compute the MS-P solution for primary drainage, both at entry pressure conditions and for continued pressure increases after invasion of the non-wetting fluid, for cross sections of arbitrary polygonal shape. The solution rests on two features.

The first is to note that, for a wetting angle, θ, of 0 degrees, the centers of curvature of the arc menisci that form the fluid-fluid interface must remain pinned on, what is known in computational geometry, as the medial axis of the polygon interior. The medial axis is a tree structure consisting of the union of curves. A smoothly varying distance function, associated with every point on the medial axis, can be used to locate each arc meniscus, both at entry pressure values (solution of the MS-P equation) and at over-pressurization values.

Fig. 4 shows the entry pressure arc-meniscus configuration for the $\theta = 0$ solution to the MS-P equation for a capillary tube cross section of irregular polygonal shape. The centers of curvature, lying on the medial axis of the

polygon interior, are also shown.

The second feature is to appropriately extend the concept of the medial axis to that of a "drainage axis" for non-zero wetting angles. Again the centers of curvature of the arc menisci must remain pinned on the (wetting-angle appropriate) drainage axis. In contrast to the medial axis, the drainage axis generally consists of disconnected curves, which can, however, still be logically organized into a tree structure. Again there exists a distance function which varies smoothly on the drainage axis; it is used to locate each arc meniscus, both at entry-, and over- pressure values. The familiar medial axis is the $\theta = 0$ limit of the drainage axis.

Fig. 4 (left) shows the drainage axis for $\theta = 30°$ for the polygon used in Fig. 4. Open points on the drainage axis indicate points that are to be considered as common when identifying its tree structure. Arc-menisci for significant points on the drainage axis are also shown. Menisci will generally exist in three "corner regions" of this polygon structure. Note that menisci drawn as dotted (rather than dashed) indicate unstable menisci configurations. Such menisci either indicate the limit in which a corner region becomes fully drained (menisci 4 and 7) or a discontinuous jump movement of the meniscus (i.e. from meniscus 11 to meniscus 5).

The geometry of the drainage axis explains and predicts, in full detail, the topological changes, pinning behavior, and discontinuous movement of menisci during primary drainage.

Using the 3DMA-Rock software, we have located and determined the geometry of over 21,500 throats in a suite of four Fontainebleau sandstone samples covering the porosity range 7.5% to 22%. In particular, the throat perimeters have been resolved as polygonal shapes (based on a digitization resolution of 5.7 microns). By modifying the medial axis software, Vroni, of M. Held (http://www.cosy.sbg.ac.at/~held/projects/vroni/vroni.html) we have computed the $\theta = 0$ entry pressure arc-meniscus configuration for all 21,500 throats. The solutions for the first 16 of the 9,294 throats in the 22% sample are shown in Fig. 6.

Our results have the following significance for network flow models. By adding a computational module (or by pre-computed lookup tables) it is possible for network flow models to compute a more exact entry pressure value for any polygonally shaped throat that may be desired in the flow model. If pore throat shapes are imperfectly known, our work verifies that Hwang's hydraulic radius approximation (the ratio A/P of throat area to throat perimeter length) provides an excellent (though slightly under-valued) prediction for the arc meniscus radius of curvature at entry pressure conditions *in real rocks.*

2 Supported Publications

At this early stage of the Stony Brook component of the work on the Viking core samples, no publications have as yet been produced. Work describing our development and application of the latest algorithmic capabilities of 3DMA-

Rock, including pore surface area, as well as our breakthrough work on arc meniscus configuration in capillary tubes of arbitrary polygonal cross section have resulted in the following publications, supported whole or in part, by this grant.

M. Prodanovic, W.B. Lindquist and R.S. Seright, Porous structure and fluid partitioning in polyethylene cores from 3D X-ray microtomographic imaging. J. Colloid Interf. Sci., submitted.
W. B. Lindquist, The geometry of primary drainage. J. Colloid Interf. Sci., to appear.

3 Figures

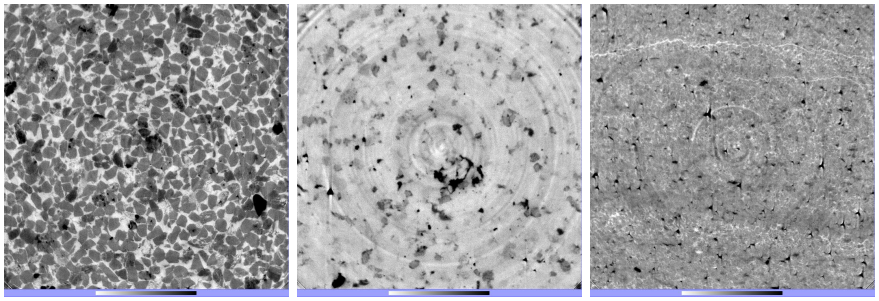

(a) 3W4 (b) 6W5 (c) 7W4

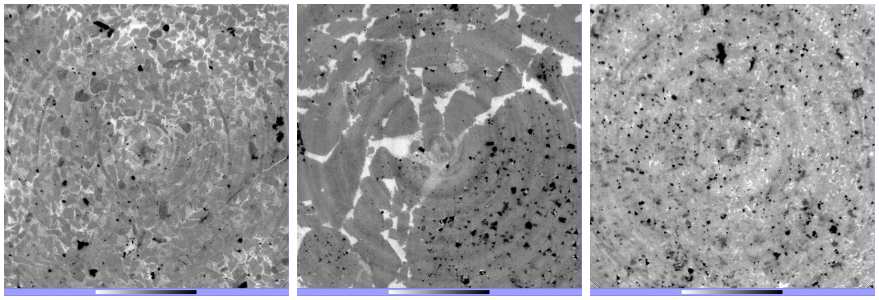

(d) 10W4 (e) 14W5 (f) 19W4

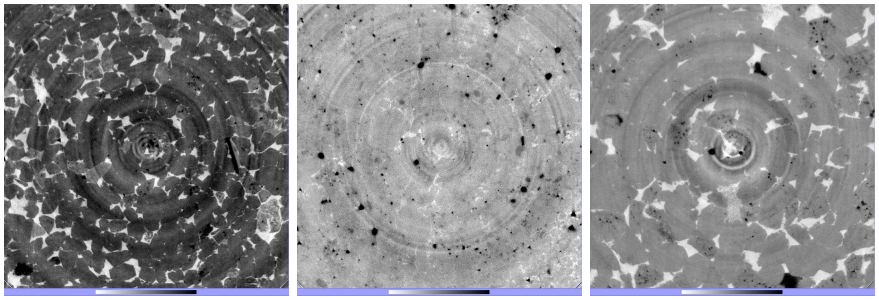

(g) 19W5 (h) 20W4 (i) 24W4

Figure 1: Image sections from 9 of the 12 Viking core samples.

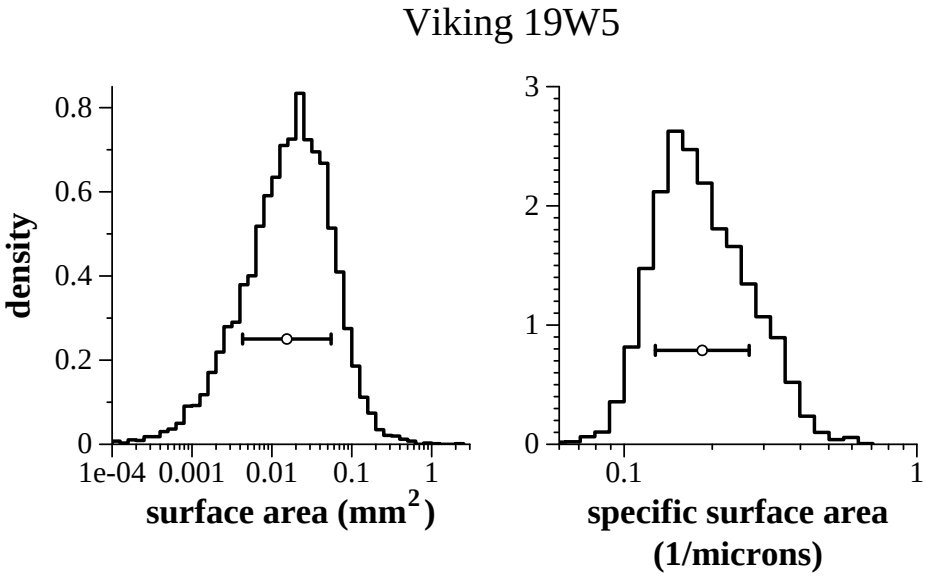

Figure 2: (Left) The distribution of pore surface areas for the pore network measured from one of the images taken from the Viking 19W5 well sample. (Right) The distribution for pore surface area normalized by pore volume. Open point with horizontal whiskers display mean and standard deviation.

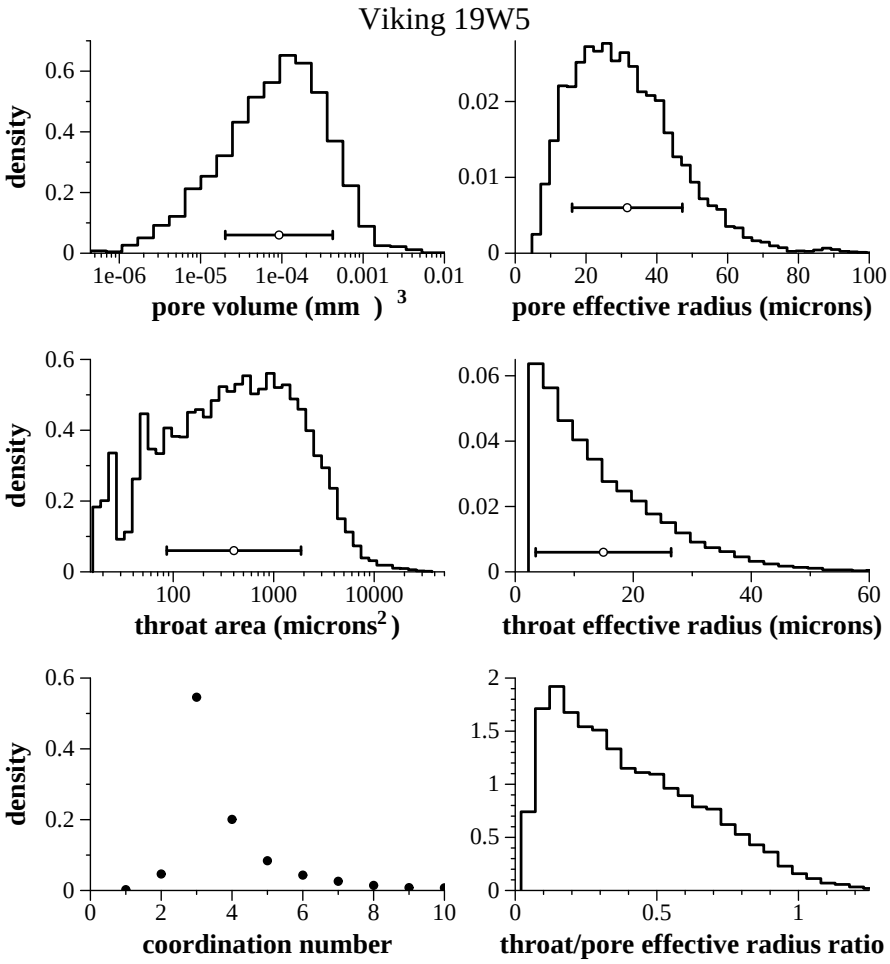

Figure 3: Distributions of (upper) pore volume and effective radius; (middle) throat area and effective radius; (lower) pore coordination number and throat:pore effective radius ratio for the same network as in Fig. 2. Open points with horizontal whiskers display mean and standard deviation.

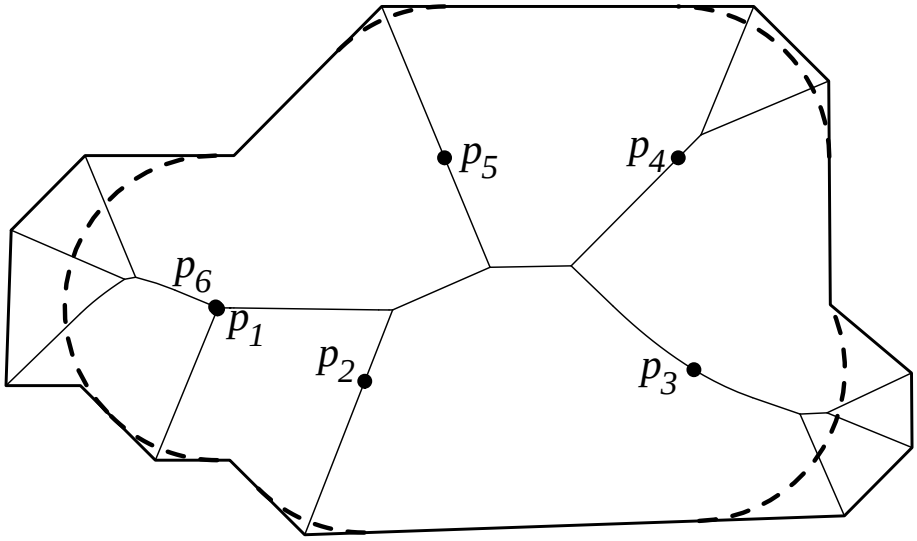

Figure 4: Arc-menisci configuration (heavy dashed curves) at entry pressure configuration for primary drainage ($\theta = 0$) into the depicted polygonal cross section. Also shows are the polygon boundary (dark solid lines) and its interior medial axis (light solid lines) along which the arc-menisci centers of curvature (labeled solid points) must be located.

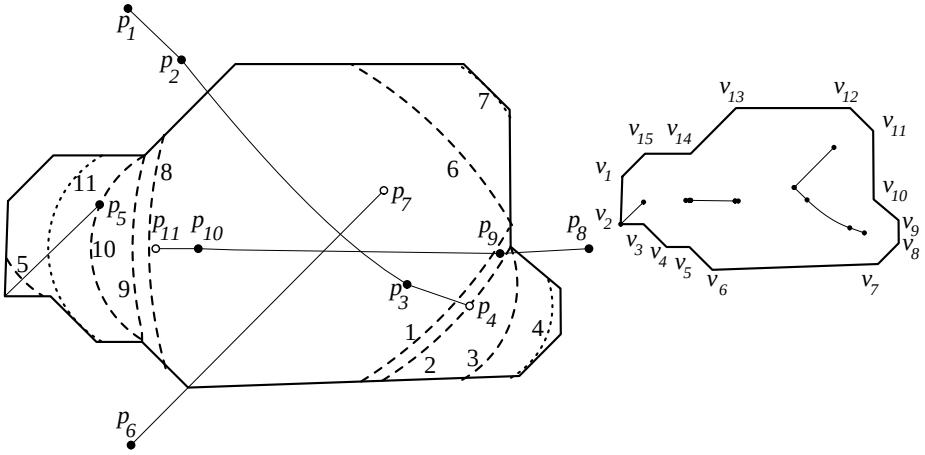

Figure 5: (left) The drainage axis for a wetting angle of 30 degrees for the polygon of Fig. 4. (right) The branches from the medial axis of Fig. 4 that correspond to branches of the drainage axis in the left figure.

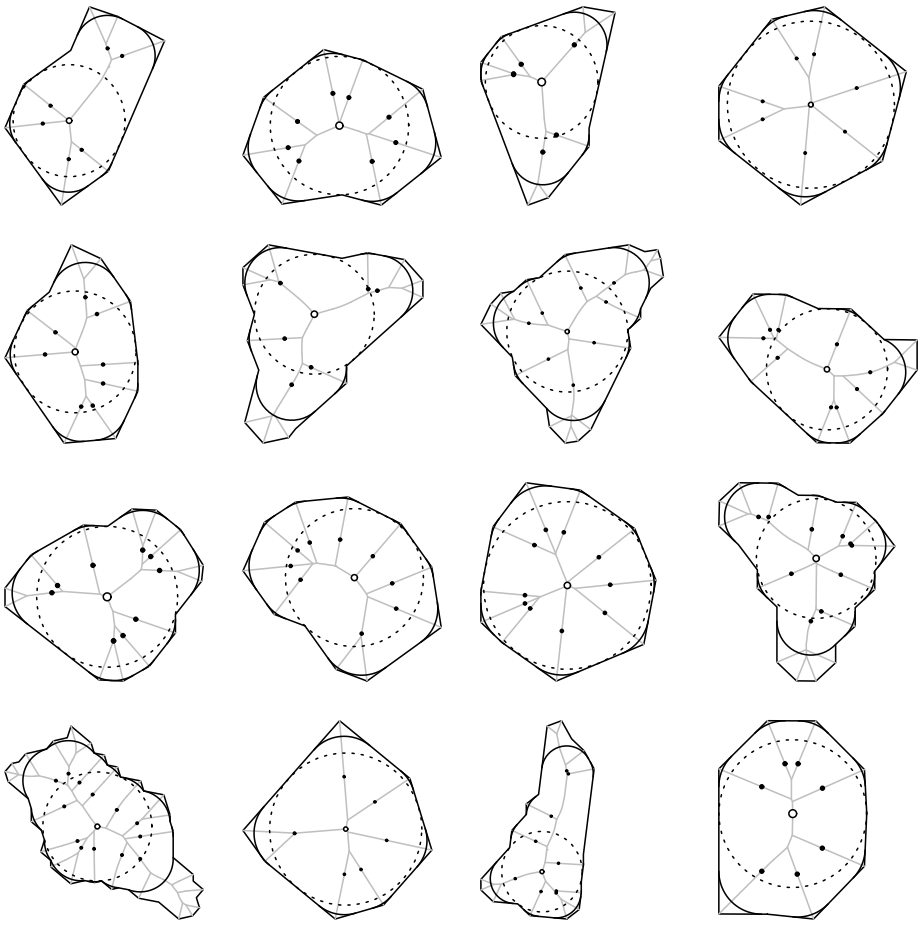

Figure 6: Arc meniscus locations (solid arcs) at entry pressure for $\theta = 0$ for the first 16 (of 9,294) throats analyzed in the 22% porosity Fontainebleau core sample image. Solid points indicate centers of curvature of the menisci. The dashed circle is the maximally inscribed circle, centered at the root location (open point) of the medial axis tree (solid gray lines).

Annual Progress Report

Up-Scaling Geochemical Reaction Rates for Carbon Dioxide (CO_2) in Deep Saline Aquifers

Grant No. DE-FG02-05ER15635 (SUNY Stony Brook)
Grant No. DE-FG02-05ER15636 (Princeton)

November 1, 2006
Budget Period: February 1, 2006 to January 31, 2007

Catherine A. Peters (P.I.)
cap@princeton.edu

Michael A. Celia
celia@princeton.edu

Department of Civil & Environmental Engineering
Princeton University, Princeton NY 08544

W. Brent Lindquist
lindquis@ams.sunysb.edu

Department of Applied Mathematics and Statistics
State University of New York, Stony Brook, NY 11794-3600

Submitted to: Nicholas B. Woodward, Project Officer
U.S. Department of Energy
1000 Independence Avenue, SW
Washington D. C. 20585-1290

Unexpended Funds:

Funds unexpended by 2/1/2007: **Princeton** $34,000.00, **Stony Brook** $7,000.00

The Princeton under-expenditure is due to the unexpected but fortunate outcome that both graduate students who are working on this project have obtained funding from other sources: one has a graduate fellowship from Princeton University and the other is a teaching assistant. This allowed us to recently bring another person onto this project, a postdoc who is doing the network modeling work. The remaining funds at the end of this budget period will no doubt be needed in the third year as both graduate students will be supported on this grant. The Stony Brook under-expenditure is due to summer salary for W.B. Lindquist, who was able to obtain matching NY State funds for partial summer salary devoted to this project.

Project Overview:

This joint project between Princeton and SUNY Stony Brook is in its second year, with a current budget period of 2/1/06 to 1/31/07. The overall goal of the project is to bridge the gap between our knowledge of small-scale geochemical reaction rates and reaction rates meaningful for modeling transport at core scales. This is being accomplished by (1) characterizing sedimentary rocks using a variety of imaging methods including CT scanning, electron microscopy and X-ray spectroscopy,

and (2) developing new pore-scale network models that combine information about rock pore structure, mineralogical characteristics, and flow properties to simulate flow and reactive transport in porous media.

This progress report covers the period 11/1/05 to 10/31/06. The primary goals of this period have been void-space and mineralogical characterization of the Viking reservoir sandstone samples (Table 1), construction of pore-networks based upon these characterizations, and development of network models for reactive flow simulations. Significant progress has been made this year, both at Princeton and at SUNY Stony Brook, which has led to both publishable findings and valuable insights on which to base the work of the third project period.

The work of the first project period has been successfully published (see list at end). In the bulk of those publications, we present the development and implementation of our first-generation pore-scale network models. We investigated the effects of heterogeneities in pore structure and mineral distribution on geochemical reaction rates in porous media. Our findings revealed significant scaling effects from variations in reactive mineral distribution, especially for the highly acidic conditions encountered in geological sequestration of carbon dioxide. Our present work is extending that work by generating and modeling realistic, not hypothetical, networks and mineral distributions.

The third year of the project will extend from 2/1/07 to 1/31/08. During that time, we plan to complete the mineralogical characterizations of the samples, fully integrate this and the pore-space characterizations into reactive network descriptions, and implement the newly-developed network models to simulate reactive transport and explore scaling relationships.

Table 1. Viking field core samples imaged by CT

Core	Depth extracted	Rock Type	Well
3W4	2289 ft	sandstone	abandoned gas
6W5	8523 ft	conglomerate sandstone	abandoned gas
7W4	806.5 m	sandstone	abandoned injection
10W4	1531 ft	shaly sandstone	abandoned gas
14W5	5128-5129 ft	conglomerate sandstone	abandoned injection
19W4	1243 m	sandstone	Gas
19W5	5128 ft	sandstone	Gas
20W4	3178-3181 ft	sandstone	abandoned oil
24W4	4618 ft	sandstone	suspended injection

1. Characterization of Sandstone Samples

A. CT Imaging. In two separate beam time allotments, one during the first reporting period of this grant, and the second occurring during this reporting period, nine core samples (Table 1) from the Viking field in the Alberta basin have been imaged. Two separate CT images (from separate sub-cores) have been taken of each core, for a total of 18 images.

The images are produced at 3.98 micron voxel size, the 7 mm sample diameters means that one image can be taken per 12-hour beam injection cycle at the X2B beam line at the NSLS at BNL. Thus during 5-day beam time allocations, at most 10 images can be collected, assuming no beam interruptions. As the core samples are cylindrical, reconstructed image slices are trimmed to a maximally incised square, producing 723 x 723 x 600 voxel (2.88 x 2.88 x 2.39 mm^3) images.

B. 3DMA-Rock Analysis. Void space image analysis using the 3DMA-Rock software package at Stony Brook has been completed on one set of the nine images. Cross sectional views from each of the core types as well as typical results of pore-space characterization for a single core were produced in the last report. The result is a pore-throat characterization necessary for input to network model simulation. We have concentrated on further quantification of the variation in pore properties of the Viking core samples.

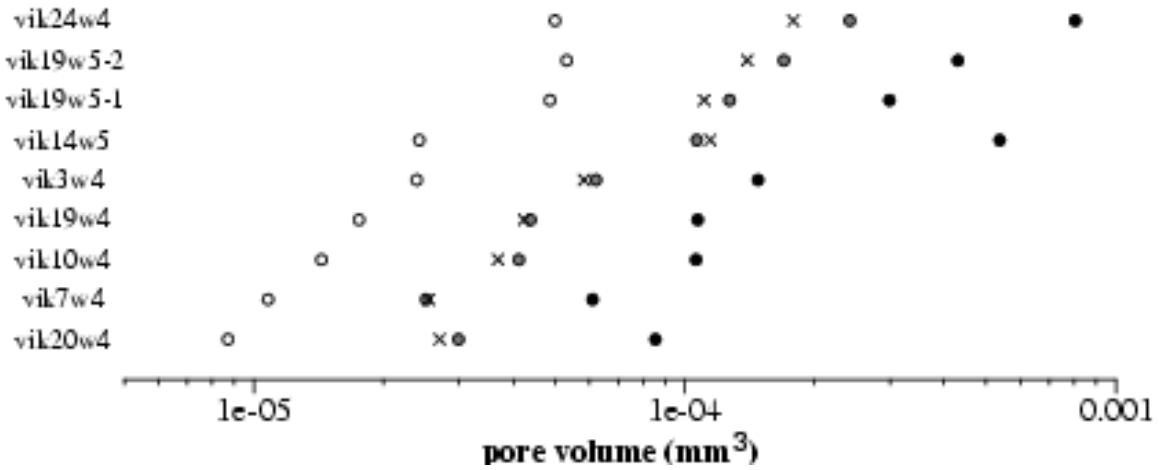

Fig. 1. Statistical summary of the pore volume distributions for the 9 Viking formation samples. Quartile values (q1: open points; q2: grey points; q3: black points) and mean values (x) are displayed for each distribution.

Of particular interest for the mineral reaction study is the amount of pore surface area available for reaction. This includes the mineral distribution component (addressed below) as well as the amount of total pore surface area available. Fig. 1 summarizes the statistics on the pore volume distributions for the first 9 imaged samples. The samples have been arranged (bottom to top) in order of increasing pore sizes. There is essentially a factor of 10 increase in typical pore size over the 9 samples.

Fig. 2 summarizes the statistics on the pore surface area distributions for the first 9 imaged samples. The samples have been arranged (bottom to top) in the same order as in Fig. 1. There is essentially a factor of 5 increase in typical surface area over the 9 samples. Since the pore volume will carry fluid mobile reactants, what is probably most critical is the amount of surface area relative to the pore volume. Fig. 3 attempts to characterize this. For a given volume, a sphere has the smallest surface area. Given a pore of measured volume V and surface area S, we compute S/S_{sphere} where S_{sphere} is the surface area of a sphere having volume V. Fig. 3 summaries the statistics on this area ratio distribution. On average, Viking pores have 1.6 to 1.9 times the available surface area that is available to a spherical pore.

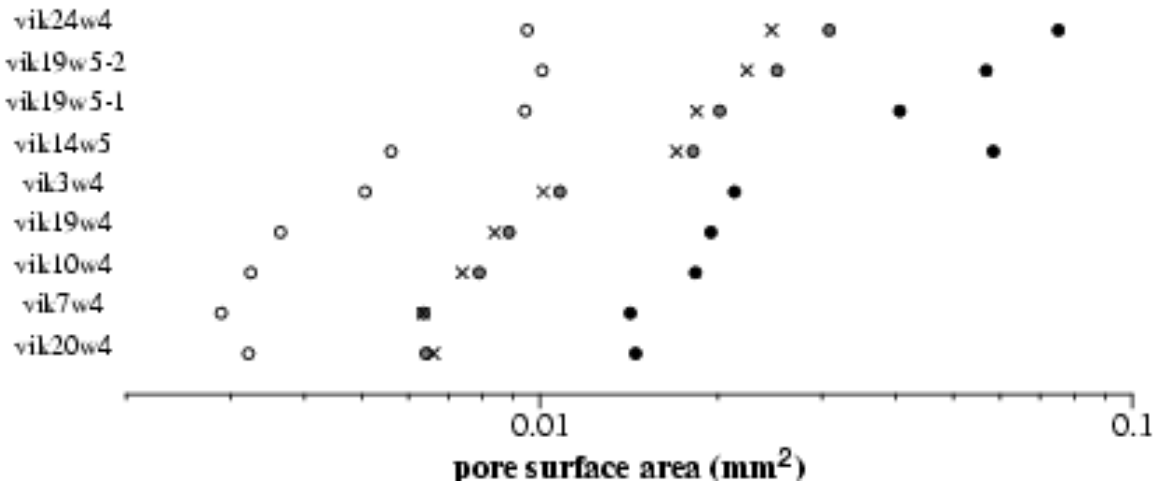

Fig. 2. Statistical summary of the pore surface area distributions for the 9 Viking formation samples. Quartile values (q1: open points; q2: grey points; q3: black points) and mean values (x) are displayed for each distribution.

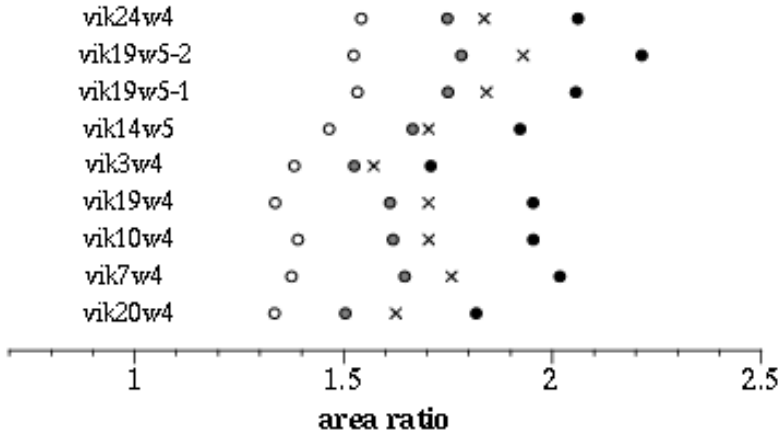

Fig. 3. Statistical summary of the S/S_{sphere} distributions for the 9 Viking formation samples. Quartile values (q1: open points; q2: grey points; q3: black points) and mean values (x) are displayed for each distribution.

It is also interesting to consider the quantification of the shapes of the pores in these samples. For each pore, we compute its principle diameters, d_1 (largest) through d_3 (smallest). By comparing the ratios d_2/d_1 and d_3/d_1, we can perform a classification of pores into sphere-shaped, crack-shaped, and ellipsoidal-shaped. The results for the samples are shown in Fig. 4. In general, 40-60% of the pores are spherical like, 30-40% are ellipsoidal, and 10-20% are crack-shaped.

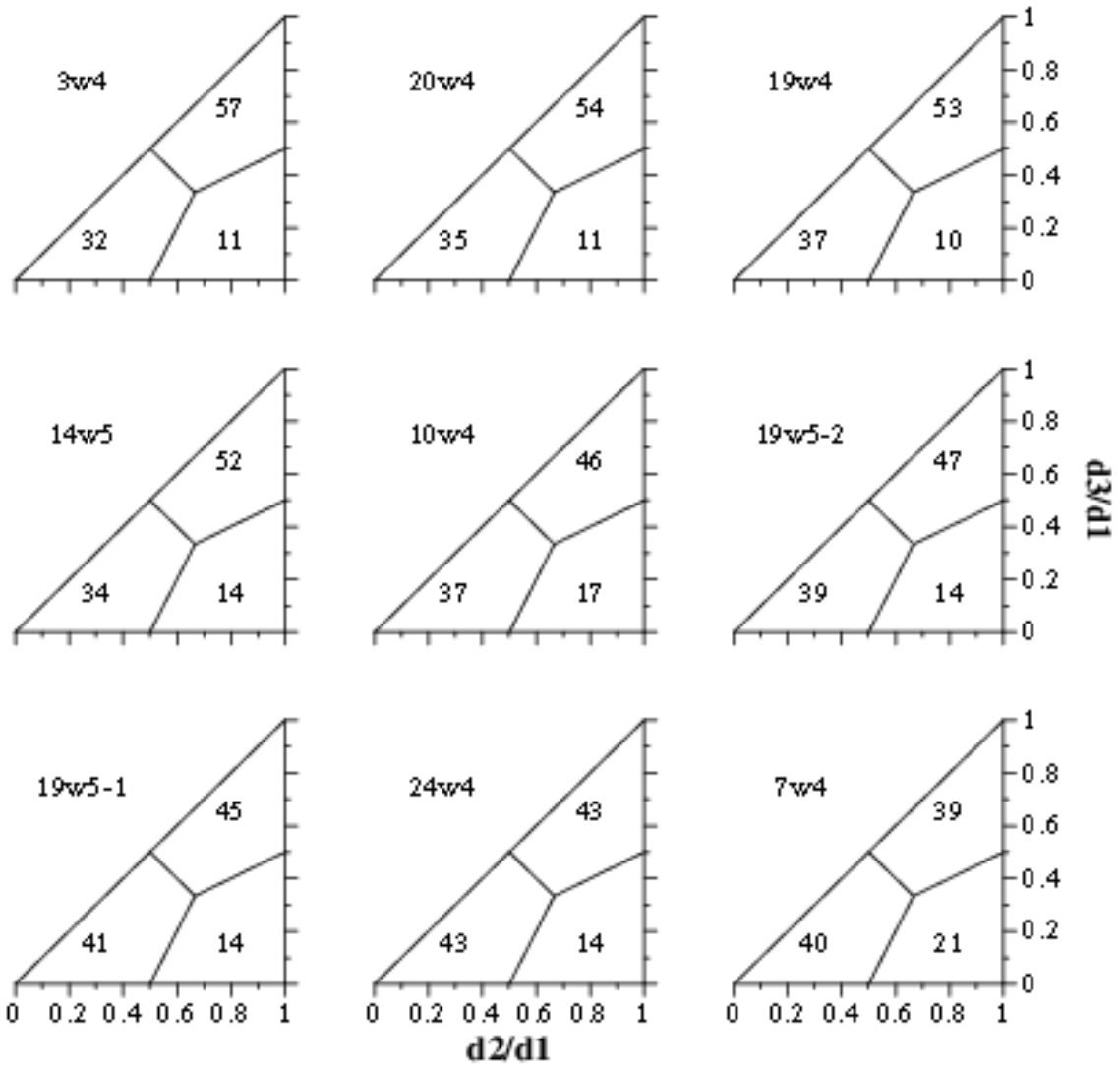

Fig. 4. Classification of pore shapes based upon ratios of principle diamaters. A pore for which $d_3/d_1 = d_2/d_1 = 1$ is spherical-shaped; $d_3/d_1 = 0$, $d_2/d_1 = 1$ is crack-shaped; $d_3/d_1 = 0$, $d_2/d_1 = 0$ is ellipsoidal-shaped. The classification can then be displayed on a ternary diagram with the classes representing the Voronoi regions associated with each vertex. Thus for Viking sample 3w4, 57% of the pores are sphere-like, 32% are ellipsoidal, and 11% are crack-like.

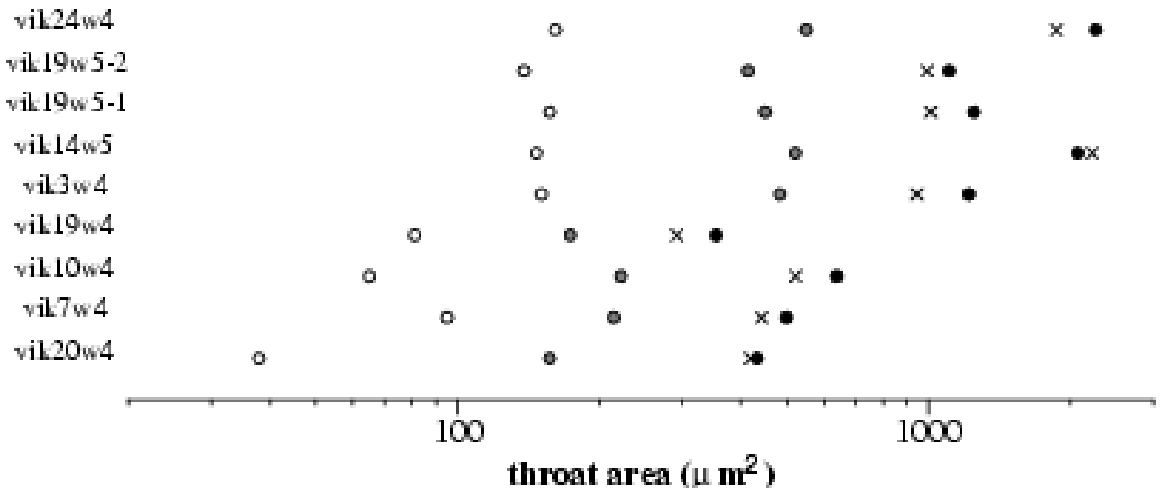

Fig. 5. Statistical summary of the throat area distributions for the 9 Viking formation samples. Quartile values (q1: open points; q2: grey points; q3: black points) and mean values (x) are displayed for each distribution.

Finally, in terms of flow, throat areas will be important in determining reactant movements from pore to pore. Fig. 5 summarizes the statistics of the pore size distributions for the 9 samples. Note, unlike for the pore volume and surface area distributions, the throat area distributions are much more skewed, with mean values generally approaching the 75% quantile (q3) value. As with pore volumes, there is roughly a factor of 10 change in average throat size across the 9 samples.

Based on coordination between Princeton and SUNY Stony Brook, we are concentrating on three of the samples, 3W4, 10W4 and 14W5, as they represent examples from the three rock types (sandstone, shaly sandstone and conglomerate sandstone) found in the sample cores.

Interestingly, in the sandstone sample, a few pores with anomalously high ($> 10^2$) coordination number have been found. A fair amount of technical work has been devoted to rechecking the pore-network construction algorithms in 3DMA-Rock to determine whether such large coordination number pores are due to (consistent) errors in constructing the network. In particular, the focus has centered on the algorithm that rejects "bad" throats. (Each rejected throat is deleted, producing pore merging and a local change in the network model.) A throat is defined to be "good" if it separates (i.e. "touches") exactly two distinct pores. As throats are constructed by 3DMA-Rock in a parallel process (i.e. the process of finding throat t_i does not depend on the existence of throat t_j, for any possible pair i,j), it is entirely possible, in the complicated geometry that real geologic media exhibit, that throats touch, or cross each other. Up to now, our algorithms have deleted one (the larger) throat in each pair that may cross. This has had the consequence of deleting some throats that only touch other throats (on their common perimeter), or cross in a many that is minimal. We are experimenting with algorithms to reclassify such throats as good. Preliminary results, however indicate that this has only mild effects on high-coordination number pores. Since such large pores occur in the conglomerate sandstone samples, we are currently investigating the possible connection between high-coordination number and mineral heterogeneity in the samples. (See the next section.)

C. Backscatter Electron (BSE) Imaging.

Thin sections of the Viking cores were prepared and analyzed using electron imaging and X-ray spectroscopy for the purpose of examining spatial patterns of mineral grains, and relating pore space with mineral interfaces. Ultimately, the goal is to quantify the abundance of minerals that would be important in the context of reactions with carbonic acid, and to determine the extent to which these minerals have contact with pore fluids. Originally, we had planned to use electron microprobe analysis to produce 2D maps of mineral content, and we invested a large amount of time during this project period to establishing our electron microprobe methodology. However, we have since found that the combination of backscatter electron (BSE) imaging, combined with energy-dispersive X-Ray (EDX) spectroscopy, provides essentially the same information. Moreover, because the information can be obtained more readily with this approach, a greater number of images can be generated leading to better statistical interpretation.

Backscatter imaging is a mode of electron microscopy that uses the high energy electrons that emerge at angles greater than 90 degrees to provide information about the mean atomic number (MAN). The resulting 2D grayscale images that are produced provide compositional contrast that indicates mineralogy of geological samples.

Fig. 6 shows backscatter electron (BSE) maps (left) of samples 3W4, 10W4 and 14W4. To visually distinguish important mineralogical features, also shown (right) is a processed version of each BSE map, where pixels have been colored according as to whether their average atomic number is less than, equal to, or greater than that of quartz; or pore-space (no scattering). Quartz typically accounts for more than 80% of the mineral matter. The “green” mineral is kaolinite (verified using EDX, see below), an authigenic precipitate that cements grains. Kaolinite is one of the few minerals with a MAN smaller than quartz, so it is easily distinguished from other non-quartz minerals that have greater backscattering and appear white in a BSE map. The minerals in this category are processed “red”, and account for 1% to 7% of the mineral matter. BSE imaging provides a useful means of evaluating the size, shape and total volume of pores in consolidated rocks. A Viking shaly sandstone has substantially less pore space than the non-shaly sandstones, and the pore space is in the form of fractures rather than interstitial space.

In conclusion, the minerals that have the greatest amount of contact with pore space are largely authigenic, mature minerals that are not likely to play a large role in further weathering reactions. The less mature reactive minerals are found among the minerals in the “red” category. These are much less abundant and less likely to have contact with pore space. This has significant implications for reactive transport modeling which typically bases mineral reaction rates on bulk abundances. A more accurate measure would be the amount of pore space in contact with reactive minerals, and this is smaller percentage than the total volume percentage. Shales and shaly sandstones have the largest abundance of reactive minerals, but reactive flow occurs in fractures rather than primary pore space. This presents a challenge to reactive transport modeling. Our ongoing work to quantify pore fluid/mineral interfaces will provide essential information for accurate modeling.

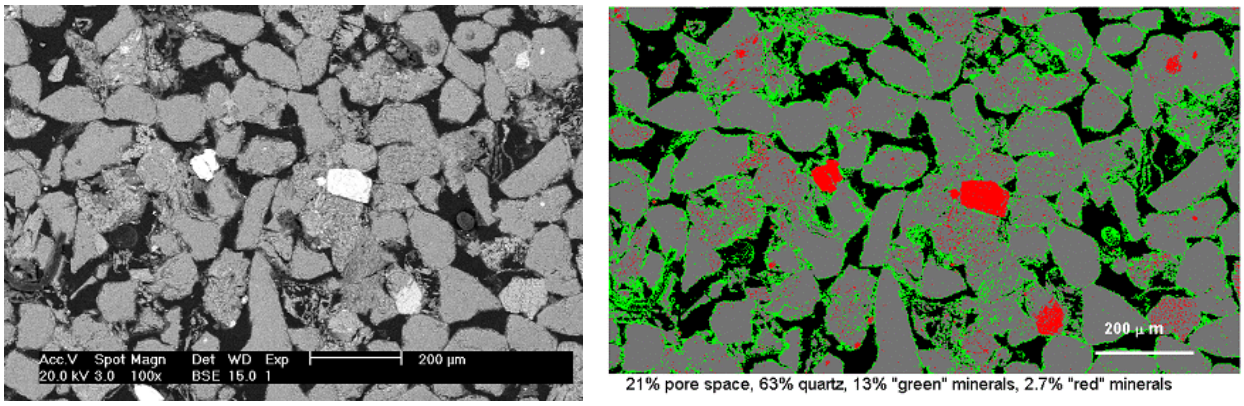

Sample 3W4, Sandstone

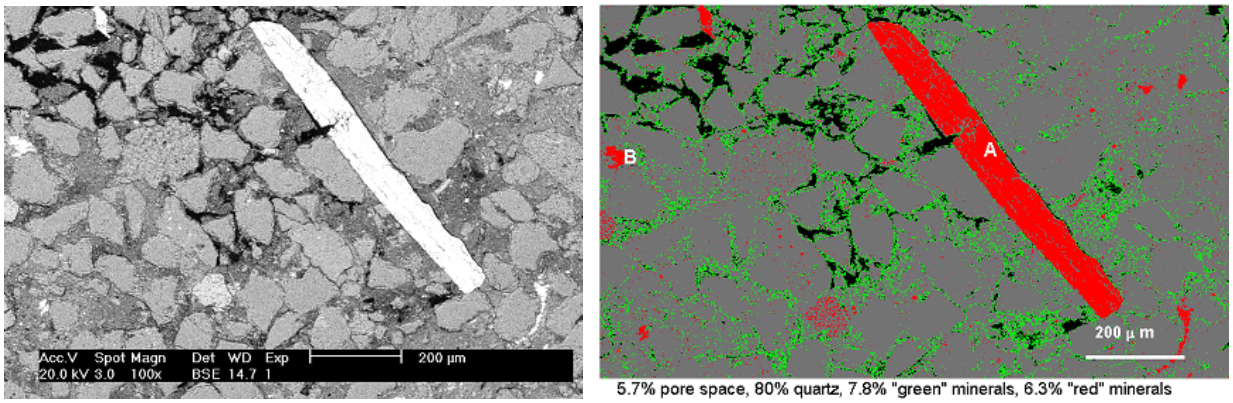

Sample 10W4, Shaley Sandstone

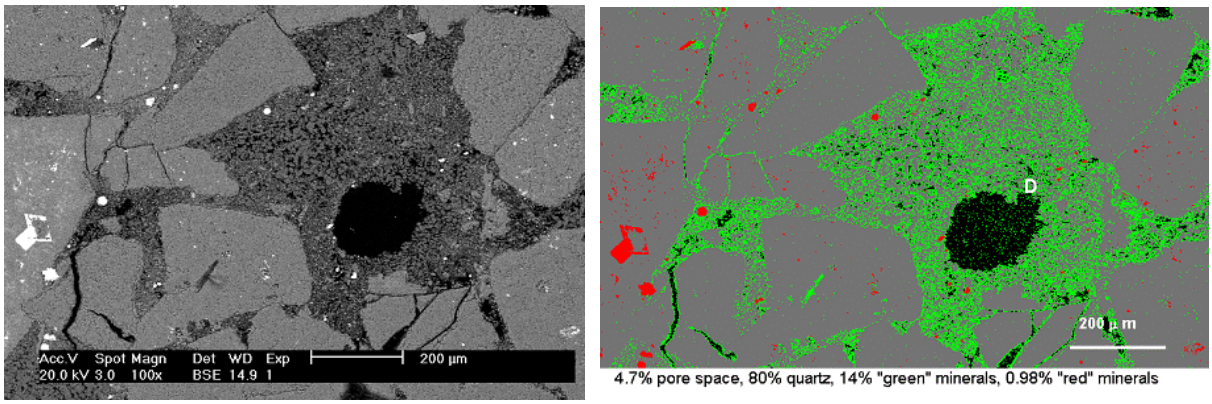

Sample 14W5, Conglomerate Sandstone

Fig. 6. (left) Backscatter electron maps and (right) images segmented according to mean atomic number (MAN) of material relative to quartz. Black: pore space, green: MAN < quartz, grey: MAN = quartz, red: MAN > quartz.

D. Energy Dispersive X-ray (EDX) Analysis. To supplement the compositional contrasting determined using BSE imaging, EDX spectroscopy is being used to identify the non-quartz minerals present at each point. The EDX results confirm that the "green-colored" minerals that cement sandstone grains are kaolinite, a clay that is produced from natural diagenesis of aluminosilicates like anorthite. Fig. 7 shows the results of a typical EDX analysis for a small region of the 14W5 conglomerate sandstone sample. Apatite and pyrite are commonly found in these samples. Other minerals that have been found contain Ca, Mg, Zn, and Ti. The EDX work is ongoing. Ultimately, the plan is to produce EDX 2-D maps that will be interpreting in a coordinated fashion with the BSE images (which have higher resolution).

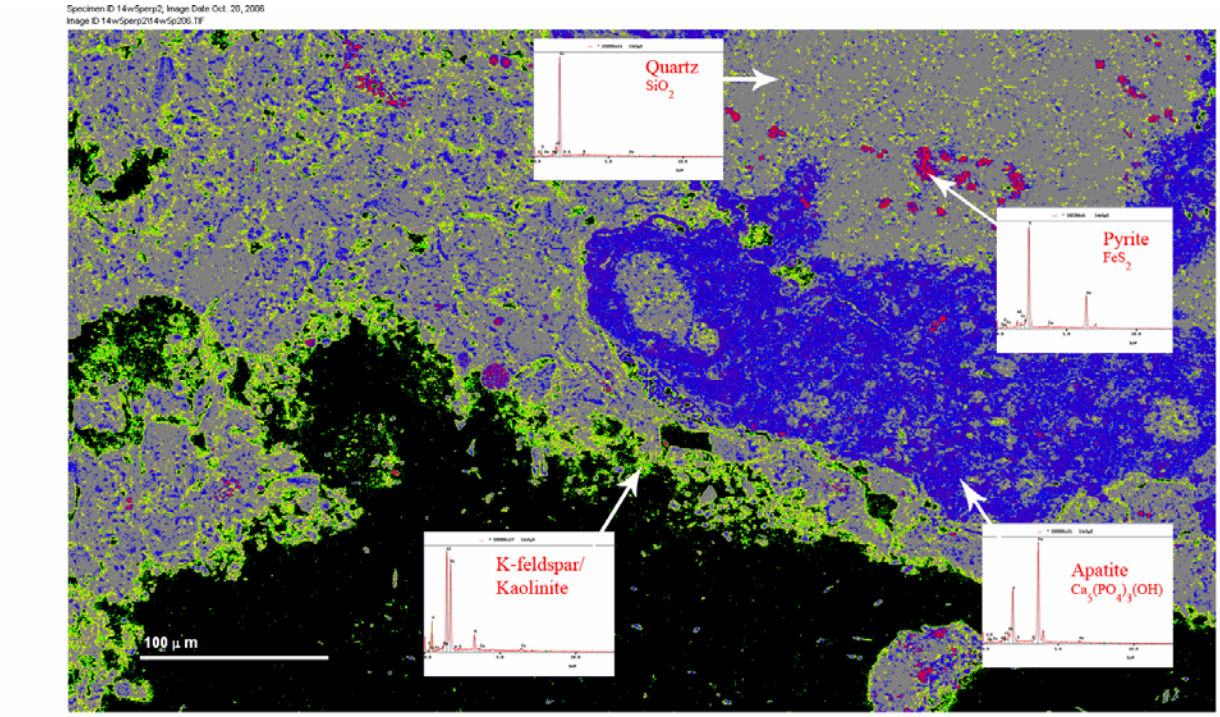

Fig. 7. Energy dispersive X-ray spectroscopic analysis of a region of sample 14W5 showing quartz and the primary non-quartz minerals, including kaolinite, apatite and pyrite.

E. Grain Surface Area "Visibility". The BSE map and EDX analysis indicates that it will be crucial to obtain statistics on the quartz surface area accessible (not coated by other minerals) in a pore. The segmented BSE maps in Fig. 6 will be analyzed using the surface area finding algorithms in 3DMA-Rock. 3DMA-Rock is set up to compute the surface area between any two segmented regions that are in contact with each other. The pore-accessible surface areas of the other major mineral species can also be computed, for consideration in other chemical reactions. This surface area analysis has just started.

2. Network Reactive Transport Modeling

A. Network Models and Reactive Transport Simulations

A second-generation pore-scale network code for single-phase steady-state reactive flow has been implemented. The model is different from our first-generation models in that it handles arbitrary connectivity of the pore network and was parameterized using the 3DMA analysis of the 3W4 rock (carried out by Dr. Lindquist). The data was checked for consistency, identifying several pores with anomalously large coordination numbers, exceeding 300-400, likely due to irregular mineral deposition. Two methods were used to estimate the conductance of pore throats: (1) a statistical approach, assuming a log-normal distribution of conductances and varying the mean/variance to match a target bulk permeability of the network (e.g., 10^{-12} m^2 for sandstone). However, many combinations of mean/variance yield the same bulk permeability, differing in the internal distribution of flows; and (2) a fluid-mechanics approach assuming spherical pores connected by a single biconical throat. This approach is currently favoured. The geochemistry module is nearly complete. The current code uses an explicit O(5) Runge-Kutta algorithm with adaptive time stepping to integrate the pore-scale reactive transport equations. The model allows for (i) advection of chemical species by the flowfield, (ii) pore-to-pore diffusion driven by concentration gradients and (iii) chemical reactions between minerals and aqueous species. The code is flexible in terms of chemical species and reactions that are modelled. We are setting up the boundary conditions and parameterisation for the minerals and aqueous species participating in the 2 kinetic and 9 equilibrium reactions in the system.

Next, we will investigate whether the pore-scale network with reactive minerals can be upscaled, and whether the system can be adequately characterised at a continuum scale using REV concepts. A single-tank "lumped" approximation will be set up. Naïve upscaling will be examined by volume-averaging the actual system parameters (ie, using the total reactive area, volume-averaged reaction rate constants, etc.). Our prior work suggests this approach is unsatisfactory, and so we will examine alternative upscaling approaches. In particular, we will determine effective macro-scale parameters by calibrating the lumped model to the pore-scale results. The stability of these effective parameters will be investigated by varying the forcing conditions (boundary flows and concentrations) and flowfield heterogeneity (varying the throat conductances). Statistical distributions of the effective parameters will also be derived empirically, allowing prediction limits to be constructed for the lumped model. If successful, this will be an important breakthrough in geochemical upscaling. In addition, since pore-scale simulations are computationally intensive, implicit integrators will be tried. The current code already implements the O(4) Rosenbrock method, but needs modification to handle sparse storage of Jacobians. Finally, domain decomposition strategies will be investigated, e.g., integrating the advection operator explicitly, the diffusion operator semi-implicitly and the reactions fully implicitly. This may reduce computational cost by minimising the number of (expensive) matrix manipulations and exploiting the fact that chemical reactions are not coupled on a pore-to-pore basis. Faster numerical simulators will allow us to use much larger networks.

B. Validation of Model Absolute Permeabilities

The network flow models used here are single phase transport models. It is therefore important that local permeability values be as accurate as is possible. Network flow models compute an effective conductance for each channel in the network based upon geometrical data. The network flow model at Princeton is based upon channels modeled as converging/diverging cylinders of circular cross section. Throat area, pore volume and surface area, and channel length data available from the 3DMA-Rock analysis are used to fit the parameters needed in the model geometry.

We have made progress on a validation mode for the conductances used in network models. 3DMA-Rock has been enhanced with the ability to run a single-phase, lattice Boltzmann (LB) computation in each individual channel (i.e. through each individual throat) in the network. These LB computations use the exact geometry of the channel local to the throat to compute flow, and hence obtain a permeability (i.e. a conductivity) for each throat. These conductivities can be used to verify the conductivities computed from geometrical models in a network flow model. The LB computations are time consuming, given the large number ($\sim 10^4$) of throats involved, but are exactly parallel, each throat computation running independent of the others. We have just begun these LB computations for the 3W4, 10W4 and 14W4 data sets.

Publications

The following publications were supported entirely, or in part, by this grant.

Li, L.; C. A. Peters; M. A. Celia. 2006. "Upscaling geochemical reaction rates using pore-scale network modeling" *Advances in Water Resources* 29: 1351-1370.

Li, L.; C. A. Peters; M. A. Celia. 2006. "Reply to 'Comment on upscaling geochemical reaction rates using pore-scale network modeling' by Peter C. Lichtner and Qinjun Kang", *Advances in Water Resources*. In Press.

Li, L.; C. A. Peters; M. A. Celia. 2006. "The Effects of Mineral Spatial Distribution on Reaction Rates in Porous Media", *Water Resources Research*. In Press.

Binning, P.J., M.A. Celia, and L. Li, "Pseudokinetics arising from the Upscaling of Equilibrium", in Proceedings of the XVI International Conference on Computational Methods in Water Resources, edited by Philip J. Binning Peter Engesgaard, Helge Dahle, George F. Pinder and William G. Gray. Copenhagen, Denmark, June, 2006 (http://proceedings.cmwr-xvi.org).

Peters, C. A., J. A. Lewandowski, M. L. Maier, M. A. Celia, L. Li. 2006. Mineral Grain Spatial Patterns and Reaction Rate Up-Scaling. Proceedings of the XVI International Conference on Computational Methods in Water Resources, edited by P. J. Binning, P. K. Engesgaard, H. K. Dahle, G. F. Pinder and W. G. Gray. Copenhagen, Denmark, June, 2006. Permanently archived at http://proceedings.cmwr-xvi.org.

L. Li, C. A. Peters, M. A. Celia. 2005. "Scaling of geochemical reaction kinetics in heterogeneous porous media using pore-scale network modeling" American Geophysical Union 2005 Fall Meeting, San Francisco. EOS Trans. AGU 86(52), Fall Meeting Supplement, Abstract B32B-04.

W.B. Lindquist. The geometry of primary drainage. *J. Colloid Interf. Sci.*, 296(2) (2006) 655-668.

M. Prodanovic, W.B. Lindquist and R.S. Seright. Porous structure and fluid partitioning in polyethylene cores from 3D X-ray microtomographic imaging. *J. Colloid Interf. Sci.*, 298(1) (2006) 282-297.

M. Prodanovic, W.B. Lindquist and R. Seright. Residual fluid blobs and contact angle measurements from X-ray images of fluid displacement. Proceedings, International Conference on Computational Methods in Water Resources XVI, Copenhagen, Denmark, June 19-22, 2006.